

MHD Stability of ISM Phase Transition Layers I: Magnetic Field Orthogonal to Front

Jennifer M. Stone¹ & Ellen G. Zweibel^{1,2}

ABSTRACT

We consider the scenario of a magnetic field orthogonal to a front separating two media of different temperatures and densities, such as cold and warm neutral interstellar gas, in a 2-D plane-parallel geometry. A linear stability analysis is performed to assess the behavior of both evaporation and condensation fronts when subject to incompressible, corrugational perturbations with wavelengths larger than the thickness of the front.

We discuss the behavior of fronts in both super-Alfvénic and sub-Alfvénic flows. Since the propagation speed of fronts is slow in the ISM, it is the sub-Alfvénic regime that is relevant, and magnetic fields are a significant influence on front dynamics. In this case we find that evaporation fronts, which are unstable in the hydrodynamic regime, are stabilized. Condensation fronts are unstable, but for parameters typical of the neutral ISM the growth rates are so slow that steady state fronts are effectively stable. However, the instability may become important if condensation proceeds at a sufficiently fast rate.

This paper is the first in a series exploring the linear and nonlinear effects of magnetic field strength and orientation on the corrugational instability, with the ultimate goal of addressing outstanding questions about small-scale ISM structure.

Subject headings: instabilities—ISM: structure—MHD

1. Introduction

The interstellar medium (ISM) exhibits structure over a wide range of size scales. In particular, so-called “small scale structure”, ranging in size from a few hundred kilometers up to parsec-scales, has been uncovered by a variety of observational techniques over the

¹Department of Astronomy, University of Wisconsin–Madison, 475 N. Charter Street, Madison, WI 53706

²Department of Physics, University of Wisconsin–Madison, 1150 University Avenue, Madison, WI 53706

last few decades. This structure manifests itself in neutral, ionized and molecular form and appears to be over-pressured with respect to the surrounding medium. Small-scale atomic structure was first revealed by a VLBI HI absorption study towards the extragalactic source 3C 147 (Dieter et al. 1976), which showed AU-scale variations in HI opacity. Other techniques to probe these variations include the use of optical tracers (particularly Na I D lines) against binary stars and globular clusters (e.g. Lauroesch et al. 1998), multi-epoch HI absorption measurements against pulsars (e.g. Frail et al. 1994), and mapping of HI optical depth against continuum sources (e.g. Faison et al. 1998). Small-scale molecular structure is revealed by observations of time-variability of molecular lines seen in absorption against quasars (e.g. Marscher et al. 1993), and small-scale ionized structures are probed using pulsar scintillation (reviewed by Rickett 1990).

At present, no single theory is able to account for all forms of small-scale structure. The challenge is to explain the observed large ranges in pressure and temperature (e.g. Jenkins & Tripp 2001) in the context of a dynamic ISM. The ISM is often described by a multi-phase model that includes the effects of supernova explosions and X-ray ionization (McKee & Ostriker 1977). A feature of this paradigm is that the various phases are in approximate pressure equilibrium. However, it is now thought that turbulence has a significant role in creating a more complex medium at small scales, featuring large contrasts in density, pressure and temperature (e.g. Kritsuk & Norman 2002; Koyama & Inutsuka 2002; Audit & Hennebelle 2005; Gazol et al. 2005; Heitsch et al. 2005; Mac Low et al. 2005). A major obstacle is that the fundamental nature of small-scale structure is not understood. The discovery of “tiny”, low column density clouds (e.g. Braun & Kanekar 2005; Stanimirović & Heiles 2005) suggests it could be in the form of discrete objects, but it is also argued that it is part of a power spectrum resulting from turbulent processes (e.g. Deshpande 2000). The pervasiveness of small-scale structure is also unknown. For example, a multi-epoch pulsar study by Frail et al. (1994) suggested that $\sim 15\%$ of the cold neutral medium (CNM) is in the form of AU-scale structure. However, more recent pulsar work (e.g. Johnston et al. 2003; Stanimirović et al. 2003) shows structure to be more sporadic and argues that previous “detections” were likely the result of systematic calibration errors. VLBA observations towards 3C 138 (Brogan et al. 2005) suggest the filling factor of atomic structure in the CNM is $\leq 1\%$. Thus, it is especially complicated to assess the degree to which small-scale structure is universal in the ISM since it is difficult to detect.

To make progress in understanding structure generation it is important to assess the relative roles of dynamical processes and those involving thermal conduction and evaporation. For example, Slavin (2007) has argued that evaporation is unimportant in dynamically active regions but that it may become dominant in quiescent regions. In this paper we examine the stability properties of evaporation and condensation fronts separating two media of different

temperatures and densities. The thermal-type corrugational instability results from perturbations that are periodic on a surface of discontinuity, causing it to wrinkle. Its character has been discussed in the context of shock waves (D’yakov 1954; Landau & Lifshitz 1987) and combustion (Williams 1964). The instability was first applied to combustion in Type Ia supernovae by Bychkov & Liberman (1995). In a study of the structure and stability of CNM/WNM phase transition layers Inoue et al. (2006; hereafter IIK06) showed that evaporation fronts are hydrodynamically unstable to corrugational deformations, whereas condensation fronts are hydrodynamically stable. It was also suggested that such perturbations could generate turbulence in the nonlinear regime within a dynamical time of the ISM. Three-dimensional hydrodynamic numerical simulations (Kritsuk & Norman 2002) suggest that the formation of filaments and voids in a multiphase ISM induce turbulence that can saturate the nonlinear thermal instability. Our primary interest here is in the potential of the corrugational instability to generate structure.

The Alfvén velocity in the neutral ISM is at least 10 - 100 times larger than the flow speed of fronts. Therefore, magnetic fields will significantly affect their dynamics. In this work we discuss the modifications to the hydrodynamic analysis for the scenario of a magnetic field orthogonal to a front, and concentrate on the sub-Alfvénic regime as the astrophysically relevant case. The linear effects of magnetic fields on combustion fronts in the context of supernovae were considered by Dursi (2004). In that work it was shown that super-Alfvénic flames are not significantly affected by a magnetic field, whereas in the sub-Alfvénic case the instability can be greatly suppressed. Dursi’s work is equivalent to our evaporation front setup, so in this paper we extend the analysis to condensation fronts.

We discuss the physical picture of fronts in §2 and present the linear stability analysis in §3. Mode analyses and dispersion relations for the super-Alfvénic and sub-Alfvénic regimes are presented in §4. The physical mechanism of the instability is discussed in more detail in §5. We apply our findings to the neutral ISM in §6, and summarize our results and mention future work in §7. In the appendices we present the derivation of the dispersion relation for the magnetized entropy-vortex wave and compare our method with that of Dursi (2004), to allow ease of comparison between the supernova and ISM applications. This paper is the first in a series exploring the linear and nonlinear effects of magnetic field strength and orientation on the corrugational instability.

2. Front Structure

We consider the physical setup of a phase transition layer (or front) separating two uniform media of different densities and temperatures in a 2-D plane-parallel geometry.

These phases result from the balance of radiative heating and cooling due to cosmic rays and external radiation fields (Wolfire et al. 2003). The nature of a front depends on the pressure. There exists a “saturation pressure” such that heating and cooling are balanced inside a static front (Zel’dovich & Pikel’ner 1969; Penston & Brown 1970). An evaporation front exists if the saturation pressure exceeds the external pressure such that there is net heating across the transition layer. In a condensation front the saturation pressure is exceeded by the external pressure such that there is net cooling across the layer. The physical setup is illustrated in Figure 1. We assume the front is located in the plane $x = 0$ with the ambient flow parallel to the x -axis and select the reference frame so that it moves with the front. A uniform magnetic field is orthogonal to the front, but has no effect on its structure since it does not exert any force and does not modify thermal conduction in the direction of the temperature gradient. We assume the perturbations on each side of the front are incompressible, since the ambient flow speed is subsonic (IIK06).

The thickness of a front (the Field length, λ_F) is given by

$$\lambda_F = \sqrt{\frac{\kappa(T)T}{n^2\mathcal{L}}}, \quad (1)$$

where $\kappa(T)$ is the temperature-dependent thermal conductivity and $n^2\mathcal{L}$ is the net cooling rate (Begelman & McKee 1990). For example, λ_F has the values 0.01 pc and 0.1 pc for the CNM and WNM, respectively (IIK06). In order to include all relevant physical processes one must consider perturbations with wavelengths both larger and smaller than λ_F . For wavelengths larger than the front thickness the transition layer is treated as discontinuous and perturbations of the fluid dynamical variables are important. This allows for a straightforward analysis but neglects the effects of thermal conduction and thermal stability (IIK06). To remedy this one must also consider corrugations smaller than the front thickness for which perturbations of the thermodynamic variables are important. In this work we only discuss the long wavelength, discontinuous front approximation. The roles of heating, cooling, and thermal conduction in front stability will be the subject of future study.

3. Phase Transition Layer Stability Analysis

We perform a linear stability analysis for fronts undergoing corrugational deformation when subject to an orthogonal magnetic field. We choose a similar method to that of IIK06, rather than that used by Dursi (2004). We provide comments throughout this paper on the commonalities of all three approaches, with a more detailed comparison provided in Appendix B. It should be noted that Dursi’s combustion front is equivalent to our evaporation front

setup, in the sense that the downstream density is lower than the upstream density. Our work is thus an extension of his in providing the stability analysis for a condensation front.

We begin by linearizing the equations of continuity, momentum conservation, and induction in the incompressible approximation to obtain

$$\nabla \cdot (\delta \mathbf{v}) = 0, \quad (2)$$

$$\frac{\partial}{\partial t}(\rho_{U,D}\delta \mathbf{v}) + \rho_{U,D}(\mathbf{v}_{U,D} \cdot \nabla)\delta \mathbf{v} + \nabla P = \frac{(\nabla \times \delta \mathbf{B}) \times \mathbf{B}}{4\pi}, \quad (3)$$

$$\frac{\partial}{\partial t}(\delta \mathbf{B}) = \nabla \times [(\delta \mathbf{v} \times \mathbf{B}) + (\mathbf{v} \times \delta \mathbf{B})], \quad (4)$$

where subscripts “U” and “D” refer to upstream and downstream, respectively. ρ , \mathbf{v} , P , and \mathbf{B} represent density, velocity, pressure, and magnetic field, and perturbed quantities are denoted by the use of “ δ ”. We assume ideal MHD and neglect diffusivity. We take the front to be in the plane $x = 0$ and assume perturbations in the (\mathbf{k}, \mathbf{B}) plane of the form $\exp[i(k_x x + k_y y - \omega t)]$, so that unstable modes have $\text{Im}(\omega) > 0$. Substituting the form of the perturbations into equations (2), (3) and (4), and taking $\mathbf{B} = B\hat{\mathbf{x}}$ (i.e. orthogonal to the front) yields the following equations:

$$k_x \delta v_x + k_y \delta v_y = 0, \quad (5)$$

$$\rho_{U,D}(-\omega \delta v_x + k_x v_{U,D} \delta v_x) = -k_x \delta P, \quad (6)$$

$$\rho_{U,D}(-\omega \delta v_y + k_x v_{U,D} \delta v_y) = -k_y \delta P + \frac{B}{4\pi}(k_x \delta B_y - k_y \delta B_x), \quad (7)$$

$$-\omega \delta B_x = k_y(v_{U,D} \delta B_y - B \delta v_y), \quad (8)$$

$$-\omega \delta B_y = k_x(B \delta v_y - v_{U,D} \delta B_y). \quad (9)$$

The perturbations are decomposed into two surface waves that are localized to the front, and two magnetized entropy-vortex waves that are advected by the flow. We adopt a notation similar to that of IIK06 and denote the surface waves upstream and downstream of the front by $\delta v_y^{(-)}$ and $\delta v_y^{(+)}$, with dispersion relations given by $k_x^{(-)} = -ik_y$ and $k_x^{(+)} = ik_y$,

respectively. The magnetized entropy-vortex waves are represented by $\delta v_y^{(s-)}$ and $\delta v_y^{(s+)}$. Their dispersion relations are given by $k_x^{(s-)} = \omega/(v - v_A)$ and $k_x^{(s+)} = \omega/(v + v_A)$, where the Alfvén speed is given by $v_A = B/\sqrt{4\pi\rho}$. The nature of these magnetized entropy-vortex waves and the derivation of their dispersion relations are discussed further in Appendix A.

The directions of propagation of the magnetized entropy-vortex waves depend on whether the flow is super- or sub-Alfvénic. In the super-Alfvénic case no magnetized entropy-vortex waves can propagate upstream, so $\delta v_y^{(s-)}$ and $\delta v_y^{(s+)}$ are both downstream perturbations. In the sub-Alfvénic regime $\delta v_y^{(s-)}$ propagates upstream whereas $\delta v_y^{(s+)}$ is a downstream perturbation. In §4 we derive separate characteristic equations for each regime.

The x -component velocity, magnetic field, and pressure perturbations can be rewritten in terms of the y -component velocity perturbations upstream and downstream of the front, using equations (5) - (9). We represent perturbed quantities as sums of the surface waves and magnetized entropy-vortex waves:

$$\delta v_y = \sum_{\alpha} \delta v_y^{(\alpha)} \quad (10)$$

$$\delta v_x = - \sum_{\alpha} \frac{k_y}{k_x^{(\alpha)}} \delta v_y^{(\alpha)}, \quad (11)$$

$$\delta B_y = \sum_{\alpha} \frac{k_x^{(\alpha)} B}{(v_{U,D} k_x^{(\alpha)} - \omega)} \delta v_y^{(\alpha)}, \quad (12)$$

$$\delta B_x = \sum_{\alpha} \frac{-k_y B}{(v_{U,D} k_x^{(\alpha)} - \omega)} \delta v_y^{(\alpha)}, \quad (13)$$

$$\delta P = \sum_{\alpha} \left[\frac{B^2 (k_x^{(\alpha)2} + k_y^2)}{4\pi k_y (v_{U,D} k_x^{(\alpha)} - \omega)} - \frac{\rho_{U,D}}{k_y} (v_{U,D} k_x^{(\alpha)} - \omega) \right] \delta v_y^{(\alpha)}, \quad (14)$$

where α corresponds to the different types of perturbation: (-),(+),(s-), and (s+). These quantities are computed upstream and downstream of the front, with the appropriate perturbations substituted for $\delta v_y^{(\alpha)}$, depending on whether the flow is super-Alfvénic or sub-Alfvénic.

To proceed, we require the jump conditions across the front. The normal and tangential unit vectors are given by:

$$\hat{n} = \hat{x} - \hat{y} \frac{\partial}{\partial y} \delta x_f, \quad \hat{t} = \hat{y} + \hat{x} \frac{\partial}{\partial y} \delta x_f, \quad (15)$$

where δx_f is the front displacement. These are used to compute the velocity perturbations normal and tangential to the front:

$$\delta v_n = \delta v_x + i\omega\delta x_f, \quad \delta v_t = \delta v_y + ik_y v_{U,D}\delta x_f, \quad (16)$$

(IHK06). The expression for δv_n includes the motion of the front itself.

The jump condition due to the continuity equation is given by

$$[\rho\delta v_n] = 0, \quad (17)$$

where $[\Psi]$ represents the jump in quantity Ψ across the front. Following IHK06, we modify this condition by assuming that the structure of the front is unchanged by a perturbation such that:

$$\rho_U\delta v_{n,U} = \rho_D\delta v_{n,D} = 0. \quad (18)$$

This is equivalent to the condition used by Dursi (2004) that both sides of the front travel with the same velocity ($[\delta v_x] = 0$ in our notation).

The $\nabla \cdot \mathbf{B} = 0$ condition implies that the normal component of the magnetic field perturbation is conserved across the front, thus:

$$[\delta B_x] = 0 \quad (19)$$

Linearization of the normal component of the momentum flux conservation equation yields

$$2\rho\delta v_n v_n + \delta P - \frac{B_n\delta B_n}{4\pi} = 0. \quad (20)$$

By invoking the continuity of δB_n the corresponding jump condition is given by:

$$\left[2\rho v\delta v_n + \delta P\right] = 0. \quad (21)$$

Linearization of the tangential component of the momentum flux conservation equation yields the jump condition

$$\left[\rho v\delta v_t - \frac{B_n\delta B_t}{4\pi}\right] = 0, \quad (22)$$

where $\delta B_t = ik_y B\delta x_f + \delta B_y$. By substituting the expressions for the velocity, pressure and magnetic field perturbations, equations (11) - (14), into the jump conditions, equations (18) - (22), we obtain the characteristic equation of the system. This is written in the form:

$$\mathbf{M}\eta = \mathbf{0}, \quad (23)$$

where the matrix \mathbf{M} is derived from the jump conditions and

$$\eta = (\delta x_f, \delta v_y^{(-)}, \delta v_y^{(+)}, \delta v_y^{(s-)}, \delta v_y^{(s+)})^T, \quad (24)$$

To obtain the dispersion relation governing the perturbations we set the determinant of \mathbf{M} equal to zero and solve for ω .

4. Mode Analysis

In this section we provide the characteristic equations for super-Alfvénic and sub-Alfvénic fronts, in terms of the density jump across the front, $r_d = \rho_D/\rho_U$, and the ratio of the downstream Alfvén speed to the downstream flow speed, $A = v_{AD}/v_D$. Super-Alfvénic fronts have $v_U > v_{AU}$ and $v_D > v_{AD}$, i.e. $\sqrt{r_d} > A$ on the upstream side and $1 > A$ on the downstream side. Sub-Alfvénic fronts have $v_U < v_{AU}$ and $v_D < v_{AD}$, i.e. $\sqrt{r_d} < A$ on the upstream side and $1 < A$ on the downstream side. A third regime, called “trans-Alfvénic” (Dursi 2004), may be identified in which the flow speed exceeds the Alfvén speed on one side, but is less than the Alfvén speed on the other side, i.e. A takes a value between $\sqrt{r_d}$ and unity ($\sqrt{r_d} < A < 1$ for evaporation, $1 < A < \sqrt{r_d}$ for condensation). The front behavior in this regime cannot be found using the methods discussed in this work, as it is possible for more waves to propagate than there are boundary conditions constraining them, and thus no unique solution exists for the initial-value problem (Dursi 2004). We argue in §6 that the sub-Alfvénic regime is of most relevance to the interstellar medium, so do not provide any further discussion of the trans-Alfvénic regime. The stability properties for both front types in the various regimes are summarized in Table 1.

4.1. Super-Alfvénic Fronts

If a front is super-Alfvénic no entropy-vortex waves can propagate upstream, so the total upstream y-velocity perturbation is simply given by the upstream surface wave:

$$\delta v_y = \delta v_y^{(-)} \quad (25)$$

Downstream, the total y-velocity perturbation is given by:

$$\delta v_y = \delta v_y^{(+)} + \delta v_y^{(s-)} + \delta v_y^{(s+)}. \quad (26)$$

The velocity, magnetic field, and pressure perturbations on each side of the front are written in terms of these total y-velocity perturbations, and substituted into the jump conditions. Collecting terms in each perturbation, the matrix, \mathbf{M} , of the characteristic equation for the super-Alfvénic case is given by:

$$\mathbf{M} = \begin{pmatrix} \omega & -1 & 0 & 0 & 0 \\ \omega & 0 & 1 & \frac{i\omega_D}{\omega}(1-A) & \frac{i\omega_D}{\omega}(1+A) \\ 0 & 1 + \frac{i\omega}{r_d\omega_D} & 1 - \frac{i\omega}{\omega_D} & \frac{i\omega_D}{\omega}(1-A)(2-A) & \frac{i\omega_D}{\omega}(1+A)(2+A) \\ i\omega_D(r_d-1) & 1 - \frac{i\omega_D A^2}{\omega + ir_d\omega_D} & -1 + \frac{i\omega_D A^2}{i\omega_D - \omega} & -1 + A & -1 - A \\ 0 & \frac{-\omega}{ir_d\omega_D + \omega} & \frac{-\omega}{i\omega_D - \omega} & 1 - \frac{1}{A} & 1 + \frac{1}{A} \end{pmatrix}, \quad (27)$$

where $\omega_D = k_y v_D$.

Taking the determinant of this matrix yields the dispersion relation:

$$\frac{[(A^2 - 1)\omega_D^2 - 2i\omega_D\omega + \omega^2][-ir_d^3\omega_D^3 + \omega^3 + ir_d^2\omega_D(\omega_D^2 + 3i\omega_D\omega + \omega^2)]}{Ar_d\omega_D(r_d\omega_D - i\omega)(\omega_D + i\omega)\omega} = 0 \quad (28)$$

This can be simplified by removing two “trivial” modes that do not cause a displacement of the front. These modes are given by $\omega = i(1 \pm A)\omega_D$. Factoring these out, the dispersion relation can be written as:

$$\omega^3 + ir_d\omega_D \frac{(r_d + 3)}{(r_d + 1)}\omega^2 + \frac{r_d\omega_D^2}{(r_d + 1)}(1 + 2A^2 - 3r_d)\omega + ir_d^2\omega_D^3 \frac{(1 - r_d)}{(1 + r_d)} = 0. \quad (29)$$

In the limit $A \rightarrow 0$ the hydrodynamic dispersion relation of IIK06 is recovered. The super-Alfvénic stability behavior is similar to that of the hydrodynamic case; condensation fronts remain stable while an unstable mode is present in evaporation fronts. As found by Dursi (2004), the growth rate of this unstable mode is slightly enhanced. We discuss the physical origin of this behavior in §5.

4.2. Sub-Alfvénic Fronts

For sub-Alfvénic fronts the upstream y-velocity perturbation is composed of a surface wave and entropy-vortex wave:

$$\delta v_y = \delta v_y^{(-)} + \delta v_y^{(s-)}, \quad (30)$$

and the downstream y-velocity perturbation is given by:

$$\delta v_y = \delta v_y^{(+)} + \delta v_y^{(s+)}. \quad (31)$$

The matrix, \mathbf{M} , of the characteristic equation for the sub-Alfvénic case is:

$$\mathbf{M} = \begin{pmatrix} \omega & -1 & 0 & \frac{i\omega_D}{\omega}\sqrt{r_d}(\sqrt{r_d} - A) & 0 \\ \omega & 0 & 1 & 0 & \frac{i\omega_D}{\omega}(1 + A) \\ 0 & 1 + \frac{i\omega}{r_d\omega_D} & 1 - \frac{i\omega}{\omega_D} & \frac{i\omega_D}{\omega}\sqrt{r_d}(A - \sqrt{r_d})(2 - \frac{A}{\sqrt{r_d}}) & \frac{i\omega_D}{\omega}(1 + A)(2 + A) \\ i\omega_D(r_d - 1) & 1 - \frac{i\omega_D A^2}{\omega + ir_d\omega_D} & -1 + \frac{i\omega_D A^2}{i\omega_D - \omega} & 1 - \frac{\sqrt{A}}{r_d} & -1 - A \\ 0 & \frac{-\omega}{ir_d\omega_D + \omega} & \frac{-\omega}{i\omega_D - \omega} & \frac{\sqrt{r_d}}{A} - 1 & 1 + \frac{1}{A} \end{pmatrix}. \quad (32)$$

There are two trivial modes, given by $\omega = (1 + A)\omega_D$ and $\omega = i(\sqrt{r_d}A - r_d)\omega_D$, which do not displace the front. Factoring these out, the dispersion relation may be written as:

$$\omega^3 - \frac{i\sqrt{r_d}\omega_D}{1 + r_d}[1 - 2A(1 + \sqrt{r_d}) - r_d]\omega^2 - \frac{r_d\omega_D^2}{1 + r_d}[1 + 2A(A - 1) + 2\sqrt{r_d}(A - 2) + r_d]\omega - ir_d^{3/2}\omega_D^3 \frac{1 - r_d}{1 + r_d} = 0 \quad (33)$$

The stability properties are the opposite of what is obtained in the super-Alfvénic case: the evaporation front is stabilized, but an unstable mode exists in condensation fronts, the growth rate of which decreases with increasing magnetic field strength. For very large magnetic field strength, as is expected for the ISM (see §6), the growth rate is approximately:

$$\omega \approx \frac{ir_d^{1/2}(r_d - 1)}{2A^2}\omega_D \quad (34)$$

This can be written in more physical terms if we assume that material crosses the front in a time of order the cooling time, given by $t_c = 5kT/2n\Lambda$, where $n\Lambda$ is the cooling rate. For our calculations we use the cooling function of IIK06, in which $n\Lambda = 2.0 \times 10^{-26}$ ergs s⁻¹ corresponds to thermal equilibrium. Assuming the most unstable scale is twice the Field length (as is found by IIK06), the growth rate is given by:

$$\omega \approx \frac{ir_d^{1/2}(r_d - 1) 2\pi n\Lambda}{2A^2 5k_B T} \quad (35)$$

The growth rates of the unstable condensation mode in the sub-Alfvénic regime are plotted as a function of A for various r_d in Figure 2. The role of the density jump across the front in driving the instability decreases in importance with increasing A .

We have also examined the eigenfunctions of the sub-Alfvénic matrix to assess the contributions of the various perturbations. The amplitudes of the entropy-vortex waves relative to the surface waves are of order A^{-3} . Thus, the instability produces very little disturbance upstream or downstream and remains localized to the front.

5. Physical Mechanism

To investigate the mechanism of the corrugational instability we begin with the simple case of a front in the hydrodynamic limit, in which evaporation fronts are unstable whereas condensation fronts are stable. Since the normal component of the velocity perturbation is zero on both sides of the front, we use equation (16) to write:

$$\delta v_x = -i\omega\delta x_f. \quad (36)$$

If $i\omega$ is a positive, real number, as is the case for evaporation fronts, the x-velocity perturbation will reinforce the displacement of the front and continue to drive the instability. In condensation fronts δv_x opposes the displacement and thus stabilizes the front. Since all growing modes have positive imaginary ω , this argument is true in general for all unstable fronts, whether super-Alfvénic or sub-Alfvénic.

Streamline curvature can also be used as a diagnostic of stability, as has been done for flame fronts in Type Ia supernovae (Dursi 2004). In that work it was argued that in regions where the streamlines “fan out”, the local flow velocity into the front is reduced and the front can propagate further ahead. We demonstrate this analytically, by calculating the angle formed between a given streamline and the front normal, to first order in the perturbation amplitude, using:

$$\sin \theta_{U,D} = \frac{\hat{n} \times \mathbf{v}_{\mathbf{U},\mathbf{D}}}{|v|} = \frac{\delta v_t}{|v|} \quad (37)$$

In the hydrodynamic case, δv_t is continuous across the front, so we have $\sin \theta_U = \delta v_t/v_U$ and $\sin \theta_D = \delta v_t/v_D$. Evaporation fronts have $v_D > v_U$, so the downstream angle is smaller than the upstream angle so the streamlines bend towards the front normal. In the case of a condensation front $v_U > v_D$ so the streamlines bend away from the normal. This is illustrated in Figure 3. In regions where the streamlines diverge the x -velocity perturbation is negative ($\delta v_x < 0$) and so the amplitude of the corrugation is enhanced.

In the case of a magnetic field orthogonal to the front, this analysis is more complicated, since the condition on δv_t is changed. We derive it using the y -component of the linearized induction equation (12) and the tangential component of the linearized momentum equation (22). We assume $\omega \ll k_x v_{U,D}$, which can be justified *a posteriori*, and write the tangential momentum balance condition as:

$$\left(1 - \frac{A^2}{r_d}\right) \delta v_{tU} = (1 - A^2) \delta v_{tD}. \quad (38)$$

Upstream and downstream angles may be compared by writing equation (38) as:

$$\frac{\delta v_{tU}}{v_U} = \frac{A^2 - 1}{\frac{A^2}{r_d} - 1} \frac{1}{r_d} \frac{\delta v_{tD}}{v_D}, \quad (39)$$

such that

$$\sin \theta_U = \sin \theta_D \frac{A^2 - 1}{A^2 - r_d}. \quad (40)$$

In the super-Alfvénic regime we consider A to be small compared to both 1 and r_d , so equation (40) becomes $\sin \theta_U \approx r_d^{-1} \sin \theta_D (1 - A^2 + A^2/r_d)$. If $r_d < 1$, the change in streamline angle across the front is increased by the magnetic field, so the instability is enhanced in evaporation fronts, as noted in §4.1. For $r_d > 1$ the angle decreases across the front so condensation fronts are stable. In the sub-Alfvénic regime, in which $A \gg 1$ we obtain $\sin \theta_U \approx \sin \theta_D [1 + (r_d - 1)/A^2]$, which is consistent with the stabilization of evaporation fronts and the slight destabilization of condensation fronts. Thus, the streamline picture explains the regimes of stability and instability found from the dispersion relations given by equations (29) and (33).

6. Application to the ISM

The structure of fronts is calculated in IIK06 by solving the energy equation while assuming thermal equilibrium at infinity. In future work we will study the effects of magnetic fields on front structure, but for now we simply use their results to examine the growth rates of unstable modes for parameters appropriate to the neutral ISM. The magnetic field strength parameter, A , can be written in terms of the upstream gas conditions as:

$$A = \frac{v_{AD}}{v_D} = \frac{B}{v_U} \sqrt{\frac{RT_U r_d}{4\pi\mu P_U}}, \quad (41)$$

where R is the molar gas constant, μ is the mean molecular weight (assumed to be unity), T_U is the temperature in the upstream gas, and P_U is the upstream pressure. The parameters corresponding to examples of steady state evaporation and condensation fronts, derived from the front calculations of IIK06, are presented in Table 2. Both types of front are sub-Alfvénic, with their dynamics dominated by the magnetic field. In this regime evaporation fronts are stable, so we now calculate the growth rate of the unstable condensation mode. Using equation (35) and the parameters given in Table 2, we find a growth timescale $t_{grow} = 1/\omega \sim 1.8 \times 10^{18}$ s. This would imply that the corrugational instability is essentially stabilized in the neutral ISM.

However, if condensation proceeds more rapidly the instability may grow within a dynamical time of the ISM. Inoue et al. (2007) argue that the condensation speed during the growth of a thermal instability that can generate clouds is of order 1 km s^{-1} . If we use this velocity with the other parameters in Table 2 we obtain $A \sim 360$. Assuming the most unstable scale is of order 0.1 pc we find a growth timescale $t_{grow} \sim 0.6 \text{ Myr}$. This would imply that the corrugational instability has a significant effect on cloud dynamics.

Since we have neglected the thickness of the front in this analysis we cannot provide further comments on the physical scale of the instability or its growth time. The full significance of the unstable condensation mode and the actual speed of the condensation process will only become apparent through completing the finite front analysis and nonlinear simulations.

7. Summary and Conclusions

We have shown that for the case of a magnetic field orthogonal to a phase transition layer unstable modes can exist in both evaporation and condensation fronts, depending on whether the flow is super-Alfvénic or sub-Alfvénic. This is in contrast to the hydrodynamic case in which an unstable mode only occurs in evaporation fronts. We demonstrated this by

deriving linear dispersion relations, given by equations (29) and (33), and from an analysis of streamline geometry near the corrugated front.

In the super-Alfvénic case the instability in evaporation fronts is enhanced from the hydrodynamic case, which is apparent from the increase in streamline bending. In the sub-Alfvénic case evaporation fronts are stabilized and it is the condensation front that is unstable. A simple formula for the maximum growth rate of the condensation front instability is given by equation (35), from which it is shown that under conditions appropriate to steady fronts in the neutral ISM the growth time is sufficiently long that such systems are effectively stable. We make the simple argument that the corrugational instability is suppressed by the rigidity of the magnetic field. However, if condensation proceeds sufficiently rapidly the growth timescale may become less than the dynamical time, such that the instability is important for cloud formation dynamics.

Forthcoming papers in this series will consider perturbations smaller than the front thickness for both orthogonal and tangential magnetic field orientations. The full significance of the unstable modes will only be revealed through studies of their nonlinear behavior. Numerical simulations will be performed to assess the nonlinear characteristics of the instability and its potential for generating small-scale structure in the ISM.

We acknowledge support from NASA ATP Grant NNGO5IGO9G, and NSF Grants AST-0507367 and PHY-0215581. We are very grateful to our anonymous referees whose recommendations greatly improved this paper. This work has also benefited from useful discussions with F. Heitsch, K. M. Hess, A. S. Hill, S.-I. Inutsuka, N. A. Murphy and S. Stanimirović.

APPENDIX A

Derivation of the Magnetized Entropy-Vortex Wave Dispersion Relation

The magnetized entropy-vortex wave is a vortical perturbation that bends magnetic field lines and generates an Alfvénic response. The derivation of its dispersion relation is provided here for the interested reader. We seek a perturbation downstream of the interface satisfying $\nabla \cdot \delta v = 0$ while including the effects of magnetic fields. The derivation is modeled after that for the unmagnetized case (Landau & Lifshitz 1987).

We begin by writing linearized equations for the entropy, pressure and magnetic field perturbations:

$$i(k_x v - \omega)\delta S = 0, \quad (\text{A-1})$$

$$i(k_x v - \omega)\delta P = -\rho c_s^2 \nabla \cdot \delta \mathbf{v}, \quad (\text{A-2})$$

$$i(k_x v - \omega)\delta B_x = -ik_y B \delta v_y, \quad (\text{A-3})$$

$$i(k_x v - \omega)\delta B_y = ik_x B \delta v_x. \quad (\text{A-4})$$

The velocity perturbations may be found using the x - and y - components of the linearized momentum equation:

$$i(k_x v - \omega)\delta v_x = -ik_x \frac{\delta P}{\rho}, \quad (\text{A-5})$$

$$i(k_x v - \omega)\delta v_y = -ik_y \frac{\delta P}{\rho} + \frac{iB}{4\pi\rho}(k_x \delta B_y - k_y \delta B_x). \quad (\text{A-6})$$

The energy and linearized induction equations (A-2,3,4) can be used to rewrite these components as:

$$\delta v_x = k_x c_s^2 \frac{(k_x \delta v_x + k_y \delta v_y)}{(k_x v - \omega)^2}, \quad (\text{A-7})$$

$$\delta v_y = k_y c_s^2 \frac{(k_x \delta v_x + k_y \delta v_y)}{(k_x v - \omega)^2} + \frac{k^2 v_A^2 \delta v_y}{(k_x v - \omega)^2}. \quad (\text{A-8})$$

Multiplying (A-7) by k_x and (A-8) by k_y and rearranging yields:

$$\left[1 - \frac{k^2 c_s^2}{(k_x v - \omega)^2}\right] (k_x \delta v_x + k_y \delta v_y) = \frac{k^2 v_A^2}{(k_x v - \omega)} k_y \delta v_y. \quad (\text{A-9})$$

The only solution that gives $\nabla \cdot \delta \mathbf{v} = 0$ is $k^2 = 0$, i.e. $k_x = \pm i k_y$, corresponding to exponentially decaying perturbations. These are surface waves.

We proceed with the derivation by taking the linearized equations of motion and induction:

$$\frac{\partial}{\partial t} \delta \mathbf{v} = -\frac{1}{\rho} \nabla \cdot \left[\delta P + \frac{\mathbf{B} \cdot \delta \mathbf{B}}{4\pi} \right] + \frac{\mathbf{B} \cdot \nabla \delta \mathbf{B}}{4\pi \rho}, \quad (\text{A-10})$$

$$\frac{\partial}{\partial t} \delta \mathbf{B} = \nabla \times (\delta \mathbf{v} \times \mathbf{B}), \quad (\text{A-11})$$

and computing the curl of these to obtain:

$$\frac{\partial}{\partial t} (\nabla \times \delta \mathbf{v}) = \frac{\mathbf{B} \cdot \nabla}{4\pi \rho} (\nabla \times \delta \mathbf{B}), \quad (\text{A-12})$$

$$\frac{\partial}{\partial t} (\nabla \times \delta \mathbf{B}) = \nabla \nabla \cdot (\delta \mathbf{v} \times \mathbf{B}) - \nabla^2 (\delta \mathbf{v} \times \mathbf{B}). \quad (\text{A-13})$$

The z -component of the curl of the induction equation is:

$$-i\omega (\nabla \times \delta \mathbf{B})_z = \nabla^2 (B \delta v_y) = -k^2 B \delta v_y, \quad (\text{A-14})$$

and the vorticity is:

$$(\nabla \times \delta \mathbf{v})_z = \frac{\partial}{\partial x} \delta v_y - \frac{\partial}{\partial y} \delta v_x = \frac{ik^2}{k_x} \delta v_y. \quad (\text{A-15})$$

Combining these yields:

$$-i\omega \left(\frac{ik^2}{k_x} \delta v_y \right) = \frac{ik_x B}{4\pi \rho} \left(\frac{-ik^2 B}{\omega} \delta v_y \right). \quad (\text{A-16})$$

The solutions to the above are $k^2 = 0$, or $\omega^2 = k_x^2 v_A^2$, so in a moving medium the dispersion relation of the magnetized entropy-vortex wave is given by:

$$(\omega - k_x v)^2 = k_x^2 v_A^2, \quad (\text{A-17})$$

where

$$k_x = \frac{\omega}{v \pm v_A}. \quad (\text{A-18})$$

This can be compared to the dispersion relation for the unmagnetized entropy-vortex wave, which is simply $k_x = \frac{\omega}{v}$.

Appendix B

Comparison with Corrugational Instability in Burning Fronts (Dursi 2004)

The effect of a perpendicular magnetic field on the linear instability of flame fronts in Type Ia supernovae was demonstrated by Dursi (2004). Here, we compare his method with ours and summarize his findings, to allow comparison between the ISM and supernova applications. The physical setup of the supernova flame front is similar to that shown by the left side diagram in Figure 1; one should consider “Phase I” to be unburned fuel and “Phase II” to be burned ash. Dursi’s x-z coordinate system is obtained by rotating ours 90 degrees about the y-axis and then 90 degrees about the z-axis. The magnetic field is orthogonal to the flame.

Dursi assumes incompressibility and that the reaction driving a supernova flame front is sufficiently exothermic such that the density of the burned material is less than that of the incoming fuel. Thus, his scenario is equivalent to our evaporation front setup. To allow ease of comparison we rewrite his notation in terms of ours. The density ratio of the unburned to burned material is given by:

$$\alpha = \frac{\rho_u}{\rho_b} = \frac{1}{r_d} \quad (\text{A-19})$$

The strength of the magnetic field is represented by the ratio of the Alfvén speed in the unburned material to the flow speed:

$$\bar{a}_u = \frac{a_u}{W_u} = \frac{A}{\sqrt{r_d}} \quad (\text{A-20})$$

The growth rate itself is given by:

$$\bar{n} = \frac{n}{kW_u} = \frac{-i\omega}{r_d\omega_D} \quad (\text{A-21})$$

It can be shown that the jump conditions we have derived and those employed by Dursi are the same. The only differences are our assumption that the front structure is unchanged by perturbations and Dursi’s additional condition that each side of a front travels at the same velocity ($[\delta v_x] = 0$). Although this is not a condition that we directly impose it is still satisfied by our eigenfunctions. The dispersion relations we present are identical to those that are derived in Dursi (2004) and can be recovered by substitution of the relations given above. We have extended Dursi’s work by giving full consideration of the behavior of condensation fronts and applying our results to the neutral ISM.

REFERENCES

- Audit, E., & Hennebelle, P. 2005, *A&A*, 433, 1
- Begelman, M. C., & McKee, C. F. 1990, *ApJ*, 358, 375
- Braun, R., & Kanekar, N. 2005 *A&A*, 436, L53
- Brogan, C. L., Zauderer, B. A., Lazio, T. J., Goss, W. M., DePree, C. G., & Faison, M. D. 2005, *AJ*, 130, 698
- Bychkov, V. V., & Liberman, M. A. 1995, *A&A*, 302, 727
- Deshpande, A. A. 2000, *MNRAS*, 317, 199
- Dieter, N. H., Welch, W. J., & Romney, J. D. 1976, *ApJ*, 206, L113
- D'yakov, S. P. 1954, *Zhurnal éksperimental'noi i teoreticheskoi fiziki*, 27, 288
- Dursi, L. J. 2004, *ApJ*, 606, 1039
- Faison, M. D., Goss, W. M., Diamond, P. J., & Taylor, G. B. 1998, *AJ*, 116, 2916
- Frail, D. A., Weisberg, J. M., Cordes, J. M., & Mathers, C. 1994, *ApJ*, 436, 144
- Gazol A., Vázquez-Semadeni, E., & Kim, J. 2005, *ApJ*, 630, 911
- Heiles, C. , & Troland, T. 2005, *ApJ*, 624, 773
- Heitsch, F., Burkert, A., Hartmann, L. W., Slyz, A. D., & Devriendt, J. E. G. 2005, *ApJ*, 633, L113
- Inoue, T., Inutsuka, S.-I., & Koyama, H. 2006, *ApJ*, 652, 1331 (IIK06)
- Inoue, T., Inutsuka, S.-I., & Koyama, H. 2007, *ApJ*, 658, L99
- Jenkins, E. B., & Tripp, T. M. 2001, *ApJS*, 137, 297
- Johnston, S., Koribalski, B., Wilson, W., & Walker, M. 2003, *MNRAS*, 341, 941
- Koyama, H., & Inutsuka, S.-I. 2002, *ApJ*, 564, L97
- Kritsuk, A. G., & Norman, M. L. 2002, *ApJ*, 569, L127
- Landau, L. D., & Lifshitz, E. M. 1987, *Fluid Mechanics* (2nd ed.; Burlington, MA: Butterworth-Heinemann)

- Lauroesch, J. T., Meyer, D. M., Watson, J. K., & Blades, J. C. 1998, *ApJ*, 507, L89
- Mac Low, M.-M., Balsara, D. S., Kim, J., & de Avillez, M. A. 2005, *ApJ*, 626, 864
- Marscher, A. P., Moore, E. M., & Bania, T. M. 1993, *ApJ*, 419, L101
- McKee, C. F., & Ostriker, J. P. 1977, *ApJ*, 218, 148
- Penston, M. V., & Brown, F. E. 1970, *MNRAS*, 150, 373
- Rickett, B. J. 1990, *ARA&A*, 28, 561
- Slavin, J. D. 2007, in *ASP Conf. Ser.*, Vol. 365, *SINS - Small Ionized and Neutral Structures in the Diffuse Interstellar Medium*, ed. M. Haverkorn & W. M. Goss (San Francisco: ASP), 113
- Stanimirović, S., Weisberg, J. M., Hedden, A., Devine, K. E., & Green, J. T. 2003, *ApJ*, 598, L23
- Stanimirović, S., & Heiles, C. 2005, *ApJ*, 631, 371
- Williams, F. A. 1964. *Combustion Theory* (Addison-Wesley Series in Engineering Science; Reading, MA: Addison-Wesley)
- Wolfire, M. G., McKee, C. F., Hollenbach, D., & Tielens, A. G. G. M. 2003, *ApJ*, 587, 278
- Zel'dovich, Ya. B., & Pikel'ner, S. B. 1969, *JETP*, 29, 170)

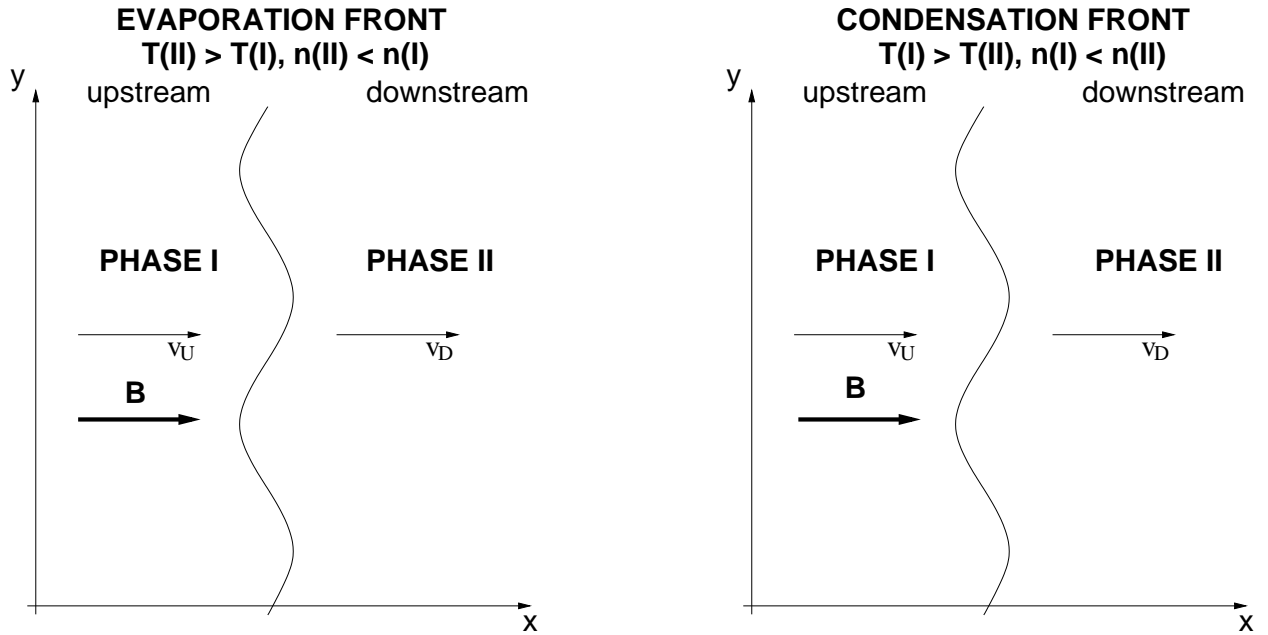


Fig. 1.— Physical setup of ISM phase transition layers undergoing corrugational deformation in a plane-parallel geometry. The regions to the left and right of fronts are identified as upstream and downstream, respectively. The phases are uniform and have different temperatures and densities. v_U and v_D are the upstream and downstream flow velocities, respectively. In an evaporation front there is net heating across the transition layer and in a condensation front there is net cooling. A magnetic field is orthogonal to the front.

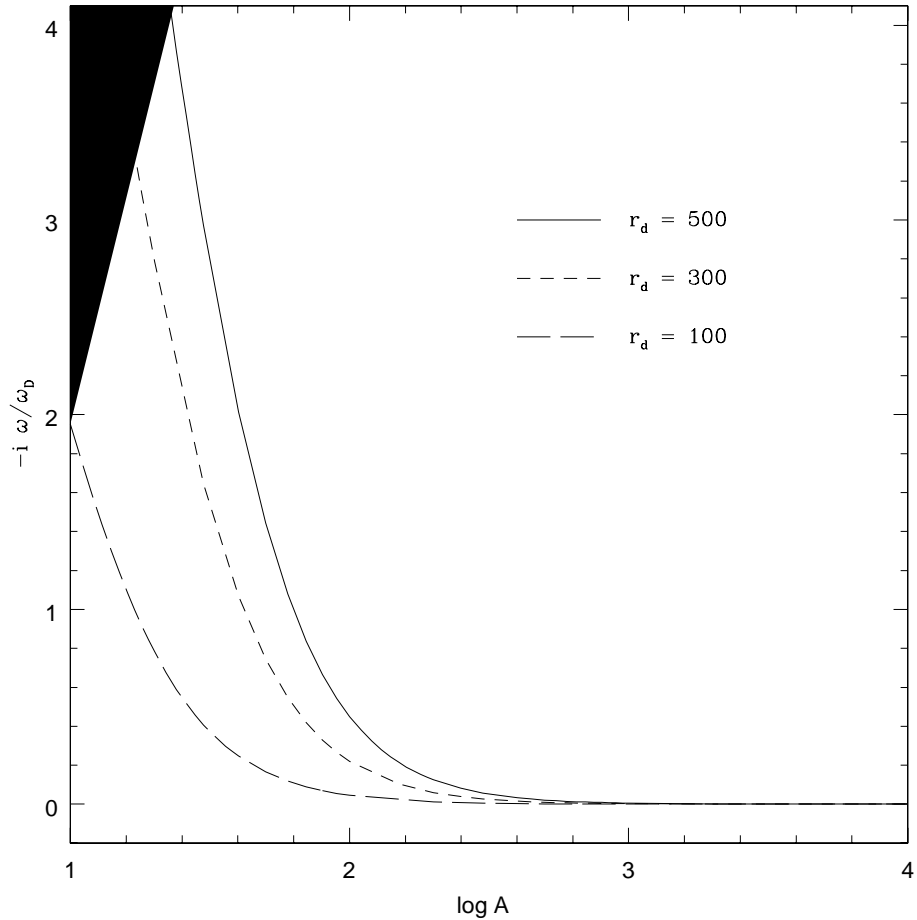


Fig. 2.— Growth rate of the unstable mode in condensation fronts of various r_d as a function of A for the sub-Alfvénic regime. The growth rate is given in units of ω_D . As the magnetic field strength is increased, the role of the density jump across the front in driving the instability becomes much less significant. For $A > 1000$, as expected in the neutral ISM, the growth rate is very slow, owing to the rigidity of the magnetic field. The blacked-out area in the top left corner covers the region of parameter space ($A < \sqrt{r_d}$) that is outside of the sub-Alfvénic regime.

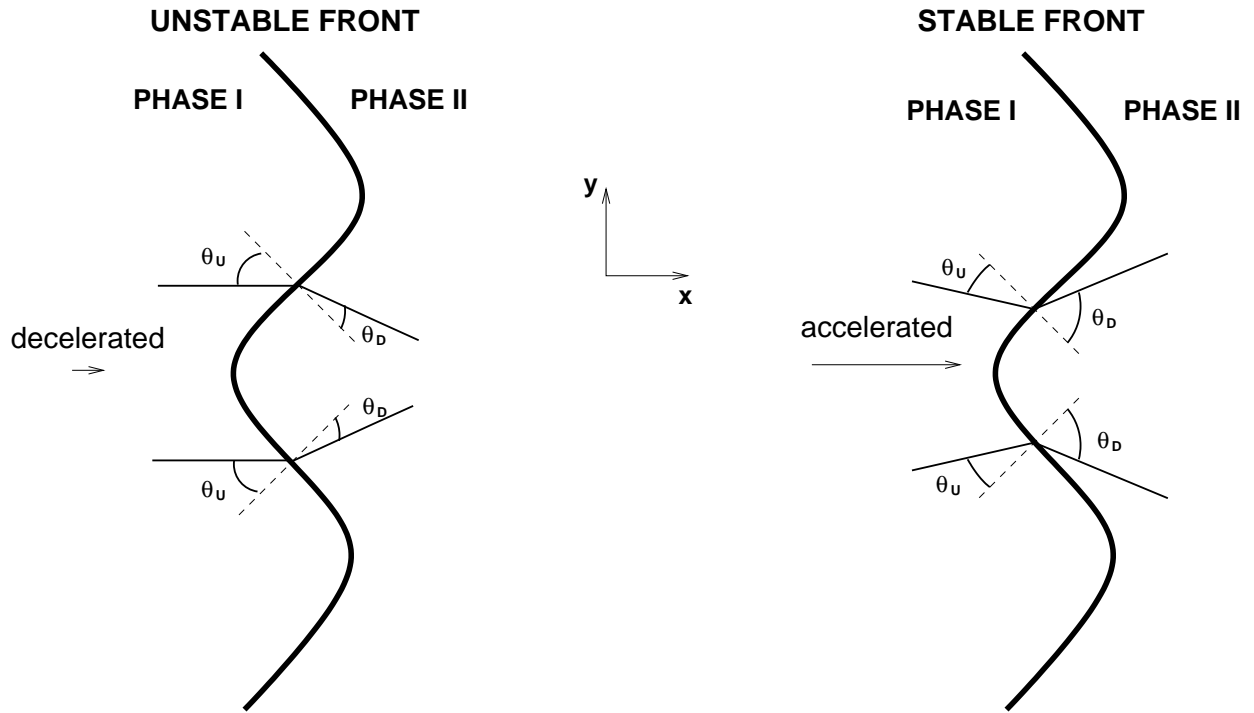


Fig. 3.— Upstream and downstream streamline angles for stable and unstable fronts. The front is represented by the thickest line and the dotted line is normal to it. θ_U and θ_D represent the upstream and downstream angles, respectively. The thin solid line represents a given streamline. In an unstable front the downstream angle is smaller than the upstream angle, so streamlines are bent towards the normal. This accelerates the front, enabling it to propagate further ahead and drive the instability. In a stable front the streamlines diverge and the corrugation is smoothed out.

Table 1. Summary of Front Stability Properties

Front Type	Hydrodynamic	Super-Alfvénic	Trans-Alfvénic ^a	Sub-Alfvénic
Evaporation	unstable	unstable	unknown	stable
Condensation	stable	stable	unknown	unstable

^aIt is beyond the scope of this work to ascertain front stability in this regime. Non-linear simulations will be required.

Table 2. Example parameters for steady state evaporation and condensation fronts in the ISM (calculated from IIK06), assuming $B = 6 \mu \text{ G}$

Front Type	P (K cm^{-3})	T_U (K)	n_U (cm^{-3})	r_d	v_U (km s^{-1})	A
Evaporation	1200	35.5	33.8	0.004	0.14	0.95
Condensation	4000	8115	0.49	371	0.0302	11,900